High frequency observation during the sand and dust storms in the Qingtu Lake Observatory

Xuebo Li[1], Yongxiang Huang[2,3,4,5], Guohua Wang[1], and Xiaojing Zheng[1]

[1]Department of Mechanics, Center for Particle-Laden Turbulence, Lanzhou University, Lanzhou 730000, People's Republic of China
[2]State Key Laboratory of Marine Environmental Science & College of Ocean and Earth Sciences, Xiamen University, Xiamen, China
[3]Fujian Engineering Research Center for Ocean Remote Sensing Big data, Xiamen, China
[4]SJTU SMSE-Mingguang Joint Research Center for Advanced Palygoskite Materials, Mingguang, China
[5]Southern Marine Science and Engineering Guangdong Lab (Zhuhai), Zhuhai, China

Correspondence: Xiaojing Zheng(xjzheng@lzu.edu.cn)

Abstract. Partially due to the global climate change, the sand and dust storms (SDS) occurred more and more frequently, yet a detailed measurement of the SDS event at different heights is still lacking. Here we provide a high frequency observation in the Qingtu Lake Observation Array (QLOA), China. The wind and dust information were measured simultaneously at different wall-normal heights during the SDS process. The datasets span the period from 17 March to 9 June 2016. The wind speed and direction are recorded by a sonic anemometer with a sampling frequency 50 Hz, while the particulate matter 10 (PM_{10}) is sampled simultaneously by a dust monitor with a sampling frequency 1 Hz. The wall-normal array had 11 sonics and monitors spaced logarithmically from $z = 0.9$ to 30 m, where the spacing is about 2 m between the sonic anemometer and dust monitor at the same height. Based on its non-stationary feature, the SDS event can be divided into three stages, i.e., ascending, stabilizing and descending stages, in which the dynamic mechanism of the wind and dust fields might be different. This is preliminarily characterized via the classical Fourier power analysis. Temporal evolution of the scaling exponent from Fourier power analysis suggests slightly below the classical Kolmogorov value of $-5/3$ for the three-dimensional homogeneous and isotropic turbulence. During the stabilizing stage, the collected PM_{10} shows a very intermittent pattern, which can be further linked with the burst events in the turbulent atmospheric boundary layer. This dataset is valuable for a better understanding of the SDS dynamics, which has being publicly available at Zenodo through the DOI 10.5281/zenodo.5034196 (Li et al., 2021a).

1 Introduction

Sand and dust storms (SDS) are common meteorological hazards not only accompanying great impacts on occurrence of acid rain (Yin et al., 1996; Terada et al., 2002) and marine biological system (Zhuang et al., 1992; Jickells et al., 2005), but also have taken harm to human health (Hefflin et al., 1994; Goudie, 2009) and led to serious air pollution (Chang et al., 1996; Borbély-Kiss et al., 2004). These phenomena can damage infrastructures, telecommunications and crops, affect transportation through reduced visibility, and cause tremendous economic losses (UNESCAPReport, 2018). According to the World Meteorological Organization (WMO), a dust storm is defined as the result of strong surface winds raising a large quantity of dust into the

air, which reduce visibility at eye level (e.g., 1.8 m) to less than 1,000 m (McTainsh and Pitblado, 1987), although severe events may result in zero visibility. The duration of SDS events varies from a few hours to several days with atmospheric PM_{10} (resp. particulate matter with a diameter 10 micrometer or less) dust concentrations beyond 15 mg/m^3 in severe events (Leys et al., 2011). Partially due to the global climate change, the SDS hazards arouse more and more concerns in recent years. Nevertheless, there is evidence to suggest that dust event frequency in Asia has been declined since the late 1970s (Shi et al., 2007). They also indicated, with the increasing vegetation cover, the decrease of the number of days with gale was the most important reason for the reduced sand-dust storms. However, it is still a big challenge to explore the abundant dynamic characteristics during SDS as a shortage of multi-height and high-frequency wind and dust information.

SDS lifts a large number of dust particles into the air and can transport them hundreds or thousands of kilometers away (Zoljoodi et al., 2013). In Northern China, as a part of Asian dust storm source, the arid and semiarid areas including sandy and gravel deserts, annually released $\mathcal{O}(10^8)$ tons of mineral dust (Laurent et al., 2006), where $6 \times 10^6 - 1.2 \times 10^7$ tons and 6.7×10^7 tons of mineral dust were transported to the North Pacific Ocean and the China Sea, respectively (Uematsu et al., 1983; Gao et al., 1997), covering a large proportion of the global mineral dust transport (Harrison et al., 2001). However, either the dust field or wind field structures during the SDS transportation are still unknown since the turbulent atmospheric boundary layer (TABL) is involved (Monin, 1970; Panofsky, 1974; Smits et al., 2011). The TABL is inherently nonlinear and has a complex interaction with other types of motion, e.g., large-scale coherent motions, gravity waves, solitary waves, low-level jets, and other nonturbulent motion (Terradellas et al., 2005; Banta et al., 2006; Holtslag, 2015; Sun et al., 2015; Wang and Zheng, 2016). For instance, it has been observed during experiments in turbulent boundary layer flows that the large-scale coherent structures contains the lengths of $2\delta - 3\delta$ [$\mathcal{O}(10^2)$ m, δ is the boundary layer thickness] in the streamwise direction (Kovasznay et al., 1970; Balakumar and Adrian, 2007). They carry a significant portion of the turbulent kinetic energy and Reynolds stress, and also play an important role in the turbulent transport process. Recently, the very large-scale motion (VLSM), also known as superstructures, whose streamwise lengths were regarded to be approximately 20δ [$\mathcal{O}(10^3)$ m] were also observed not only in channel flow, but also in TABL (Hutchins and Marusic, 2007; Smits et al., 2011; Hutchins et al., 2012). Since its discovery, the VLSM has been attracted more and more attentions (Balakumar and Adrian, 2007; Hutchins and Marusic, 2007; Wang and Zheng, 2016; Wang et al., 2017). For example, recent results show that such contained considerable energy structures were also existed and increased with heights (Hutchins et al., 2012; Wang and Zheng, 2016). Notably, Zhang and Zheng (2018) found that the space charge density and dust concentration were significantly correlated over the 10-min timescales. Therefore, the complex mechanic system during the SDS raises a great interest to investigate what kind of structures will exist and how the structures will be evolved.

However, free access to a high-frequency observation database on SDS is still lacking, which is partially due to the observation difficulty. In this work, we present high-frequency observation data from the Qingtu Lake Observatory, Minqin China, where the wind speed, wind direction, air temperature and PM_{10} are simultaneously recorded at 11 heights during a strong SDS for 24 hours, i.e., from 4:00 am 03/28/2016 to 4:00 am 03/29/2016. A preliminary result on the spectral feature during the SDS is presented. This dataset is valuable for a better understanding of the SDS dynamics. We hope the community can be

benefited from this dataset, which has being publicly available at Zenodo through the DOI 10.5281/zenodo.5034196 (Li et al., 2021a).

The site and experimental set-up description are given in section 2. Details of meteorological wind velocity, air temperature, PM_{10} concentration and quality control can be seen in section 3. Then, the basic properties of the process of the sand and dust storm are deployed in section 4, including vertical and temporal spectral structure of the fluid and dust field. Finally, section 5 presents a short conclusion of previous works based on the current site, as well as a discussion on nonstationarity of the SDS and log-law or power-law of Wind Speed against of the height.

2 Site description and measurements
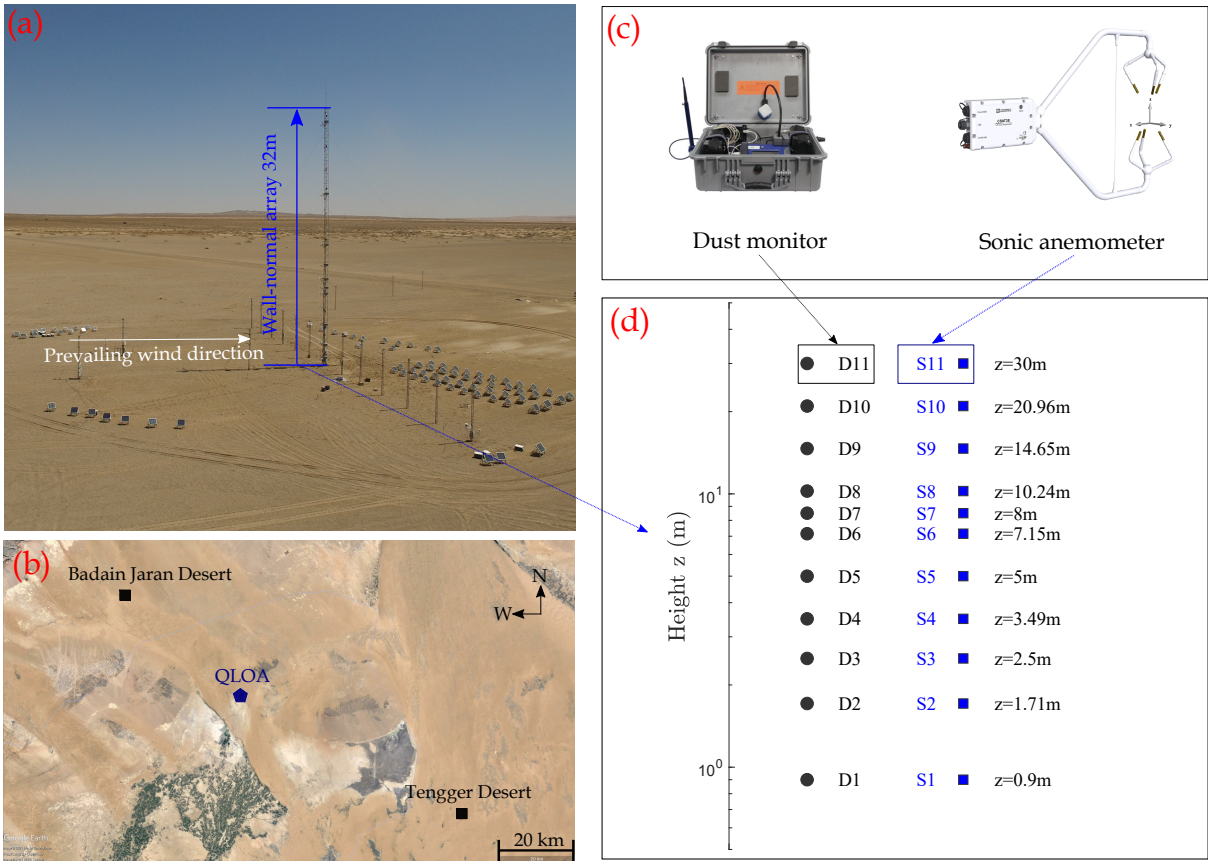
Figure 1. The field observational site and measurement array. (a) West view of the measurement array installed at the QLOA site. (b) QLOA site (high-frequency dust events in spring) is located between the Badain Jaran Desert and the Tengger Desert (© Google Earth). (c) reflects the photos of experimental instruments (dust monitor and sonic anemometer). (d) The southeast view of the sonic anemometers (square) and dust monitors (circle) array (note that the spacing is about 2 m between the sonic anemometer and dust monitor at the same height).

A field experiment was carried out on Qingtu Lake (青土湖) in Minqin (民勤), China (N: $39°12'$, E: $103°40'$) to measure the three-dimensional velocity and temperature in streamwise, spanwise and wall-normal directions in the atmospheric boundary layer. The Qingtu Lake Observation Array site is between the two of the largest deserts in China: the Badain Jaran Desert (巴丹吉林沙漠) and the Tenger Desert (腾格尔沙漠), which lies within a dusty belt in the Hexi Corridor (河西走廊) (Wang et al., 2018). One reason to choose this location is to avoid the influence of human activities, e.g. the nearest city is around 74 km far from this observation site, see the geolocation indicated in Fig.1 (b). Dust weather in Hexi Corridor is often caused by intense frontal systems. A combination of large-scale weather pattern and topological effects led to the development of the intense frontal system (Shao and Dong, 2006). Dust events occur most frequently in spring (e.g. two-thirds of the dust events occur in March, April and May). To access the vertical structure of the dust, dust monitor probes anemometers were installed at 11 heights in Fig.1 (d) in a logarithmic manner for $z =$ 0.9, 1.71, 2.5, 3.49, 5, 7.15, 8.5, 10.24, 14.65, 20.96, 30 m, respectively. At each height, a sonic anemometer (Campbell CSAT-3B, a sampling frequency of 50 Hz) and a dust monitor (TSI DUSTTRAK 8530, a sampling frequency of 1 Hz) were installed on both sides of the main tower (as shown in Fig.1 c). All the sonic anemometers and dust monitors were installed on the towers to synchronously measure the wind velocity, the air temperature and the PM_{10} concentration, over the period from 17 March to 9 June 2016.

After the passage of a cold front, the outbreak of strong wind is often accompanied by dust emissions in the spring of the northern China. On March 28, 2016, a dust storm that has passed the observation site and been recorded successfully by the aforementioned instruments, e.g., the wind and temperature data were collected from the 11 sonic anemometers as well as the PM_{10} data were obtained from synchronous 11 dust monitors for continuous 24 hours (from 4:00 am 03/28/2016 to 4:00 am 03/29/2016, UTC+08:00) at different heights below 30m. The sample size are $4,320,000$ data points for the wind velocity and temperature, $43,200$ for the dust.

As shown in Fig. 2(b), the measured wind direction was from a mess to a relatively stable status, and evolving mess again at the last. Fig. 2(a), (c), (d) and (e) represent the horizontal (U), wall-normal (W) velocity, the air temperature(T) and PM_{10} concentration, respectively. The maximum wind speed is 13 m/s recorded at z=5 m (larger at higher height) and the highest level of PM_{10} concentration reached 3 mg/m^3 (larger at a lower height). It shows strong fluctuations for U and W in the mature stage of this SDS, which is accompanying the violent PM_{10} transportation. The dataset has being publicly accessed in Zenodo data repository (10.5281/zenodo.5034196) in a Hierarchical Data Format (HDF) file, which is readable by the popular software, e.g., Matlab, Python, etc (Li et al., 2021a).

3 Data and Methodology

3.1 Meteorological wind velocity

While installing, the coordinate of the anemometer sonic (Campbell CSAT-3B), i.e., x, y and z, were in accordance with the observation array, i.e., a 45 degree angle with the northerly direction, see Fig. 3. To retrieve the meteorological wind component
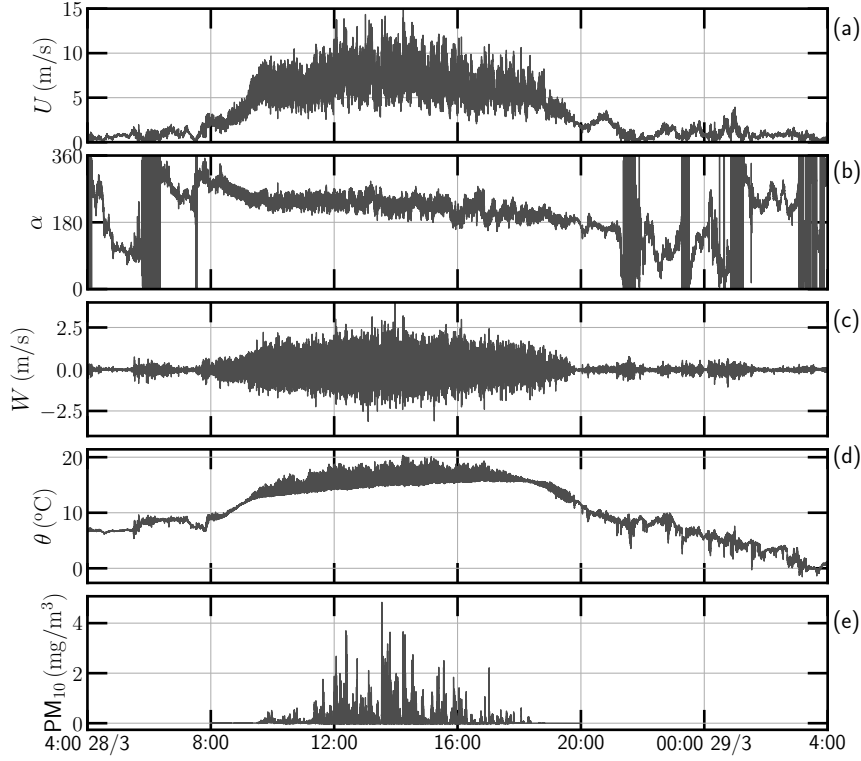
Figure 2. The measured parameters during the dust storm from 4:00 am 03/28/2016 to 4:00 am 03/29/2016: (a), (c) horizontal wind speed (m/s), vertical wind speed (m/s); (b) wind direction (α=0 corresponding to the northwestern direction, and it is positive when the wind direction varied in the clockwise direction); (d) and (e) denote temperature ($^{\circ}$C) and PM_{10} concentration(mg/m^3). Note data are from the height $z =3.49$ m.

95   from the measured wind velocity components u_x, u_y and u_z, the following equations can be applied,

$$u = (u_x + u_y)\sqrt{2}/2, \quad v = (u_y - u_x)\sqrt{2}/2, \quad W = u_z \tag{1}$$

where u, v and W are the easterly, northerly and vertical components. The wind direction is then calculated as

$$\alpha = 180 + \frac{180}{\pi}\text{atan2}(v,u) \tag{2}$$

All parameters obtained are at a sampling frequency of 50 Hz. The measurement resolution is 0.001 m/s for u_x and u_y,
100   0.0005 m/s for u_z, respectively. The wind direction can be defined from 0° to 360° with an accuracy of $\pm0.7^{\circ}$ at a typical horizontal wind speed 1 m/s. Fig. 2 (a), (b) and (c) shows the observed meteorological wind speed U, wind direction α and vertical wind velocity W at the height of 3.49 m.

Figure 3. Illustration of the observation coordinate: u_x and u_y are the wind vector measured by the anemometer, which has an 45 degree angle against the northerly direction. The corresponding meteorological wind vector and direction can be retrieved via the equations (1-2).

3.2 Air temperature

In addition, the sonic provides also the air temperature with the same sampling frequency as the wind velocity, and a measurement accurate $0.025°C$. Fig. 2 (d) shows the collected air temperature with visible outliers, which can be further excluded in analysis using different quality control strategies.

3.3 PM$_{10}$ concentration

The dust monitor (TSI DUSTTRAK 8530) collected the PM$_{10}$ with a sampling frequency 1 Hz. The PM$_{10}$ concentration is on the range 0.001 to $400\,\mathrm{mg/m^3}$ with a typical accuracy $\pm0.1\%$ or $\pm0.001\mathrm{mg/m^3}$. As aforementioned, the measured PM$_{10}$ concentration is on the range 0 to $5\,\mathrm{mg/m^3}$ with an ascending and descending stages that each lasting for few hours, see Fig2 (e). Due to the technique reason, the dust sensor at the height 5 m failed to record the data.

3.4 Quality control

In most instances it is necessary to take many natural factors and events into account, for instance, fierce buoyancy (heat flux) variance, sand and dust movement, to list a few. Quality control methods are necessary to guarantee a good quality of the data. Generally, the raw data collected from the instrument were necessary to be carried out by the pre-processing methods, otherwise, they could be misunderstood as 'trustworthy'. Typically, there are generally three types (i.e., missing and unrecognizable characters; extreme value; values greater than 'four standard deviations') needed to be pre-processed from the

raw data. For the current measurement, there is very few 'bad' data, see temperature curve in Fig. 2 (d). Therefore, we provide only the raw data with the quality control code.

120   In general, the following steps can be applied directly to the raw data to remove the outliers. i) For the 'missing' and 'unrecognizable characters': The situations for 'data missing' are rare, but the 'unrecognizable characters' in the raw data emerge sometimes while the low-battery condition, collector (Campbell CR3000) full load, or the GPS update. If the irregular point occurs with single, then it was replaced by the mean value on both sides. Otherwise, for some continuous series (less than 1 second, 50 points under the sampling frequency with 50Hz), they were replaced by the mean values based on the regular

125   points in one hour. Last, the irregular points greater than 1 second, should be considered carefully to use this data series; ii) For the extreme value (for instance, velocity component great than 100 m/s and temperature with 100 °C). Actually, extreme value occurs generally with a single point, and it is rare during the observation. It is replaced by the mean value on both sides; iii) For the values greater than 'four standard deviations': Generally, the quality control for the database adopts 'Three-Sigma Limits' to produce items of the highest quality, where the data are within three standard deviations from a mean to set the upper and

130   lower control limits in statistical quality control charts. Other methodologies are also possible to detect outliers, for instance, instead of the 'Four standard deviations', one can apply the Hampel identifier to detect the outliers (Davies and Gather, 1993). In this study, to reduce the bias from the interpolation of the data, we replace the outliers by Not-a-Number (NaN).

4   Basic Properties

In this section, we present the basic properties of the observed SDS. Without further clarification, the collected data at the

135   height of 3.49 m is presented.
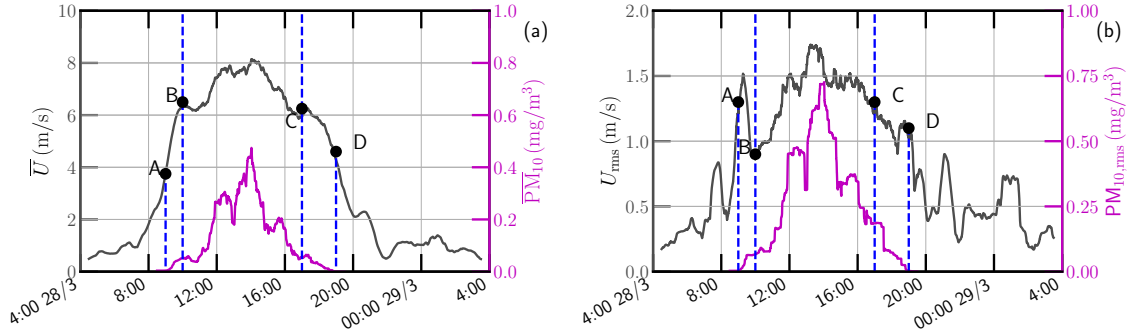
Figure 4. (a) Hourly averaged wind speed $\overline{U}$ and $\overline{PM}_{10}$ at the height of 3.49 m. (b) The corresponding root-mean-square value. This SDS event is roughly divided into three stages, which are illustrated by A-D, see main text for more detail.
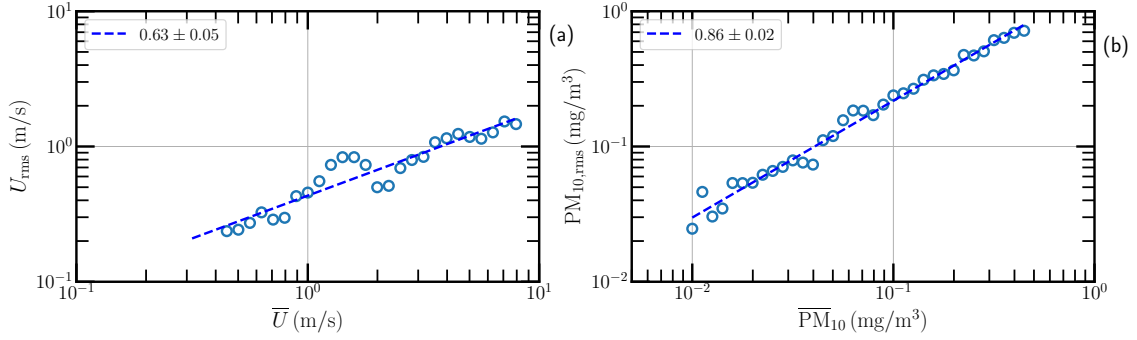
Figure 5. (a) Phase diagram of the hourly averaged wind speed versus the root-mean-square speed at the height of 5 m. (b) The hourly averaged concentration PM_{10} versus its root-mean-square value. The circle is the bin average value with 10 bins of each decade in the logarithmic scale.

4.1 Nonstationarity

As mentioned above, the SDS event is a typical nonstationary event. Fig. 4 (a) shows the hourly averaged curves for both wind speed (U) and PM_{10}, and (b) the corresponding root-mean-square values at the height of 3.49 m. Based on these curves, the observed SDS event can be roughly divided into three stages: i) the ascending stage between 9:00 am (denoted by A) and 10:00 am 28/03/2016 (denoted by B). During this stage, the wind speed increases quickly, while the PM_{10} starts to rising; ii) the stabilizing stage between 10:00 am and 17:00 pm (denoted by C). In this stage, one has the strongest wind, lasting for approximately 7 hours. The corresponding PM_{10} accumulates quickly and reaches its peak value (e.g., $PM_{10} \geq 0.35 \, \text{mg/m}^3$) maintaining for roughly 3.5 hours; iii) the descending stage between 17:00 pm and 19:00 pm (denoted by D), where both the wind speed and PM_{10} are descending sharply. The root-mean-square curves display a similar pattern. Note that a nonlinear trend is evident, see Fig. 4 (a). When calculating the root-mean-square value, a constant value is subtracted from the raw data set within a one-hour sliding window, the trend can not be fully excluded (Wu et al., 2007).

Another possible explanation of the above observed patter is the amplitude modulation due to the existence of the aforementioned VLSM that observed in the TABL with typical spatial scales from $\mathcal{O}(10^2 \, \text{m})$ to $\mathcal{O}(10^3 \, \text{m})$ (Wang and Zheng, 2016), or typical temporal scales from $\mathcal{O}(1 \, \text{min})$ to $\mathcal{O}(10 \, \text{min})$ (Wang et al., 2017). The small structures, thus the root-mean-square value, are then modulated by the VLSM (Marusic et al., 2010). This feature is further illustrated as a diagram (hourly averaged value versus the root-mean-square ones) in Fig. 5. Power-law trend is observed with scaling exponent 0.63 and 0.86 for the wind speed and PM_{10} respectively.

4.2 Vertical structure

The QLOA is in the logarithmic layer of the TABL, in which the wind speed should vary logarithmically with height that often up to $\mathcal{O}(10^2 \, \text{m})$, even to $\mathcal{O}(10^3 \, \text{m})$ (Stull, 1997). Fig. 6 (a) shows the hourly averaged speed $\overline{U}$ versus h in a semi-log view to emphasize the log-law at four time periods from A to D. It suggests that no matter the intensity of the wind speed, the log-law
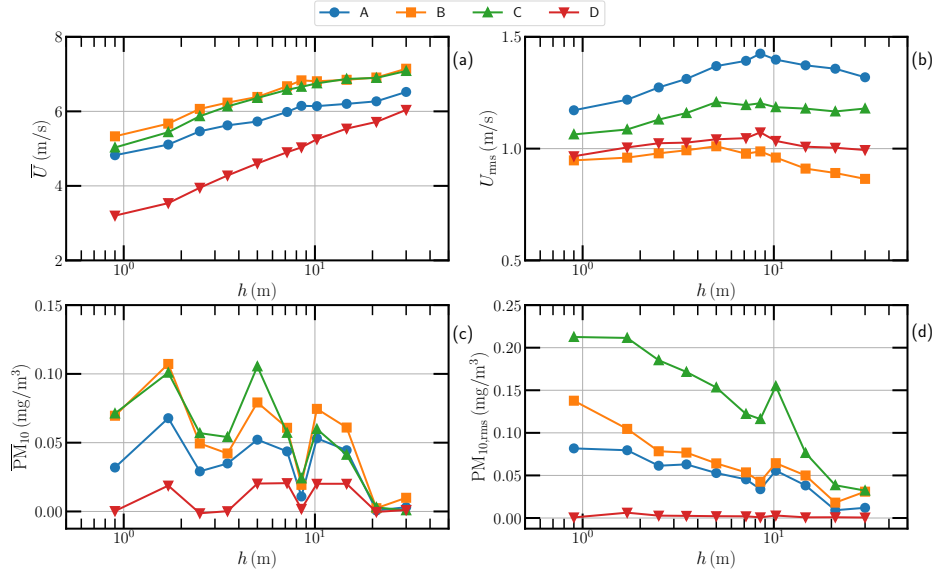
Figure 6. (a) Hourly averaged wind speed $\overline{U}$ versus height h at the same four periods as in Fig. 5. (b) The corresponding root-mean-square speed. (c) Hourly averaged concentration $\overline{\text{PM}}_{10}$ and (d) the corresponding root-mean-square one.

of the wall is preserved, which is deeply associated with the TABL. However, the corresponding U_{rms} shows a complex h-dependence. It first increases logarithmically with h and reaches its peak, e.g., $h = 8\,\text{m}$ at A, then decreases roughly logarithmic with h. There is no clear h-dependence when $h \leq 20\,\text{m}$ for the collected $\overline{\text{PM}}_{10}$ in Fig. 6 (c). While the corresponding $\text{PM}_{10,\text{rms}}$ shows a clearly logarithmic decreasing against h when $h < 10\,\text{m}$. This is partially due to the interaction between the suspended particles with the turbulent structures, which for sure deserves a further investigation.

4.3 Temporal spectral structure

In this work, the Fourier power spectra $E(f)$ are estimated via the Wiener-Khinchine theorem without involving the classical Taylor frozen hypothesis to convert the time measurement to a spatial one (Frisch, 1995). More precisely, the Fourier transform of the autocorrelation functions $\rho(\tau)$ as follows:

$$E(f) = \mathcal{R} \int_{-\infty}^{+\infty} \rho(\tau) \exp(-j2\pi f\tau)d\tau, \tag{3}$$

in which $\mathcal{R}$ means real part, $j = \sqrt{-1}$ is the complex unit, and,

$$\rho(\tau) = \frac{1}{M(\tau)} \sum_{i=1}^{M(\tau)} \widetilde{\theta}(t_i + \tau)\widetilde{\theta}(t_i). \tag{4}$$

where $\widetilde{\theta}(x_i) = \theta(x_i) - \langle \theta(x_i) \rangle$ is the centered $\theta(x_i)$, θ is the value of either wind speed U or PM_{10}, and $M(\tau)$ is the sample size at the time separation scale τ, and $\langle \cdot \rangle$ means time average. With this approach, the estimated Fourier spectrum can recover
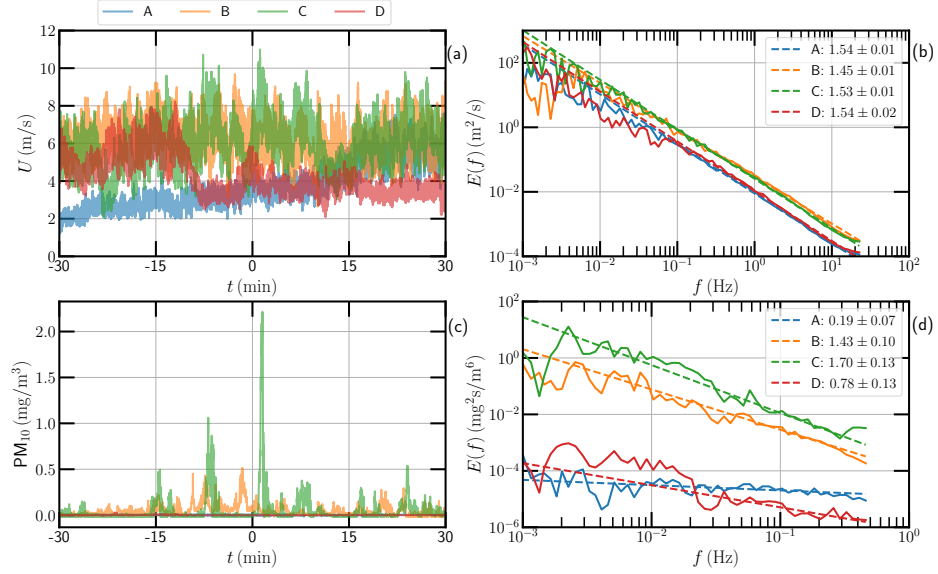
Figure 7. (a) One hour segment of the raw wind speed around time A, B, C and D at the height of 3.49 m. (B) The corresponding Fourier power spectrum. (c) and (d) The PM$_{10}$ and their Fourier spectra at the same height and time period. The dashed line is the power-law fit for reference.
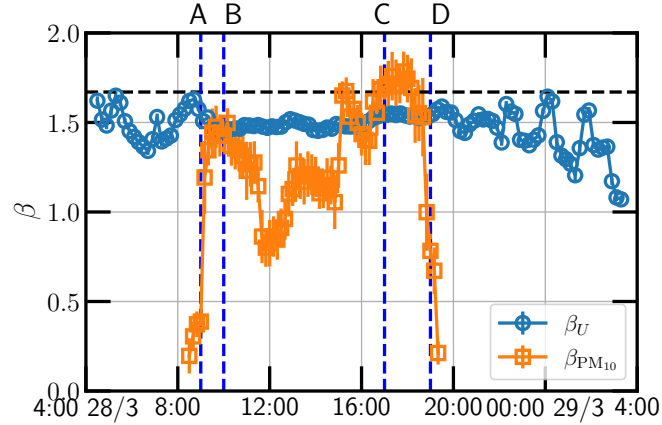
Figure 8. Temporal evolution of the scaling exponent β, which is estimated on a one-hour sliding window with 80% overlap. The horizontal dashed line indicates the Kolmogorov value $5/3$ for reference. The vertical dash line Figure 4 indicates three different stages.

the correct power-law behavior for the time series with the missing data or irregular time steps without the bias from the interpolation of the data (Gao et al., 2021).

Fig. 7 (a) shows the one-hour segment of the raw wind speed U around the typical time periods from A to D at the height of 3.49 m. Fourier power spectra $E(f)$ are then estimated using the above-mentioned Fourier spectrum estimator, see Fig. 7 (b). Due to the existence of the atmospheric turbulence, power-law behavior, i.e., $E(f) \propto f^{-\beta}$, is observed on the frequency range $0.1 \leq f \leq 10$ Hz with a scaling exponent around 1.53, which is slightly below the classical Kolmogorov value of $5/3$ for the three-dimensional homogeneous and isotropic turbulence (Frisch, 1995). This is partially due to the influence of the ground that the scaling exponent β_U demonstrates a height dependence. It seems that, except for the intensity of the wind speed, this small-scale scaling feature remains unchanged during the SDS, see Fig. 8.

Concerning the concentration of PM_{10}, the scaling feature is more complex, see Fig. 7 (d) and also Fig. 8 for the temporal evolution of the scaling exponents $\beta_{PM_{10}}$. Note that the density ratio of the sand particle and air is around $2650/1.25 \simeq 2100$ (Kok et al., 2012). Therefore, the weak wind can not blow the sand particle into the air. The scaling exponents are then approaching to zero before ascending and after descending periods. During the stabilizing stage, the collected PM_{10} shows a very intermittent patter, which can be further linked with the burst events in the TABL, see Fig. 7 (c). It is interesting to see the power-law behavior is still preserved, even more close to the Kolmogorov value, see Fig. 8 for the measured scaling exponent β versus time.

5 Discussions

The QLOA site is a one-of-a-kind field observational station that can monitor three-dimensional TABL flows (streamwise, spanwise, and wall-normal directions) for both wind-blown sand movement and clean wind, as well as the electric field near the ground surface. The facility's unique measuring array allows us to investigate the three-dimensional shape of coherent structures, as well as the temperature fluctuations that accompany them, which are also covered in this paper. Precious works where the data were collected at the current site can be categorized by three series: i) Canonical atmospheric turbulent boundary layer: The near-neutral atmospheric surface layer can be viewed as a truly high-Reynolds-number facility ($Re_\tau = \delta u_\tau / \nu = O(10^6)$, where δ is the boundary layer thickness, u_τ is the skin-friction velocity and ν is the kinematic viscosity). Characteristics of coherent structures were investigated under near-neutral and stratified conditions (e.g., Wang and Zheng, 2016; Liu et al., 2019; Li and Bo, 2019a; Li et al., 2021b). Roughness effects were explored to illustrate the features in the near surface layer (e.g., Li and Bo, 2019b; Li et al., 2021c). ii) Sand-laden flows: Wind-blown sand movements are topically two-phase flow in the arid and semiarid regions, where the interaction between flow features and PM_{10} concentration were previously discussed (e.g., Wang et al., 2017, 2020). iii) Electric field during SDS: Granular materials are regularly brought into contact or collision with one other during dust events such as blowing sand, dust devils, and dust storms, generating huge quantities of electrical charge on their surfaces. Measurements of electrical effects in dust events (especially dust storms) have been made specifically, and been further analyzed (e.g., Zhang and Zhou, 2020a, b). Notably, Wang et al. (2020) explored the comparison of large–scale structures of turbulent flows in the atmospheric surface layer with and without sand. According to the research, the streamwise

turbulent kinetic energy is enhanced at all scales in the sand-laden flows, and the inclination angles of large–scale structures are shown to increase with sand concentration, owing to the decreased velocity gradient. However, the streamwise length scale of large–scale structures and the size of the most energetic turbulent structures are found to be unaltered compared to clean-air flows. The abundant mechanisms during the SDS are still unknown, especially the difference between the variables during SDS days and those during normal days, which is necessary to be explored in detail in the future.

Dust aerosols, being one of the most important types of atmospheric aerosol constituents, have gotten a lot of attention because of their effects on the environment, weather, and climate via radiation and precipitation (Sokolik et al., 2001; DeMott et al., 2003; Zhou et al., 2021). The high resolution data collected in current work can benefit researchers to improve the current sand and dust storm model, as well as the interaction between coherent structures in the flow field and dust filed.

5.1 Nonstationarity of the SDS

In general, the TABL shows both a daily and seasonal variations due to the rotation and evolution of the earth. Therefore, not only the height of the TABL, but also its scaling feature, e.g., scaling of the wind speed, air temperature, etc., shows a daily and seasonal variations. Within a day, the wind speed, air temperature, etc., are often showing an intraday trend, see Fig. 4. As aforementioned, it is thus a typical nonstationary event. There exists more rigorous approaches to characterize or analyze the nonstationary time series. For example, a stationary parameter can be defined to characterize quantitatively the nonstationarity (Foken et al., 2004; McCullough and Kareem, 2012). One can apply also the either wavelet-based techniques (e.g., wavelet leader, synchrosqueezed wavelet transforms, etc.,) (Flandrin, 1998; Lashermes et al., 2005; Daubechies et al., 2011) or Hilbert-Huang transform (Huang et al., 1998; Wu et al., 2007; Huang et al., 2008) to extract the local time-frequency information.

It is worth to point out that the detrending methods should be applied with cautions since the trend is difficult to define, and is difficult to separation too (Wu et al., 2007). For example, when calculating the momentum transport (i.e., also known as the Reynolds stress) in a wavy aquatic environment, different approaches may provide notable different values (Bian et al., 2018). Therefore, the data-driven approaches, such as wavelet, Hilbert-Huang transform, etc., that can adaptive separate the variations into different scales are recommended to deal with the nonstationary SDS data.

5.2 Log-law or power-law of Wind Speed

As mentioned above that the wind speed is often showing a logarithmic increasing against the height h that up to few hundreds above the ground, which has been verified in current site (such as, Wang and Zheng, 2016; Liu et al., 2017). The main assumption of log-law is that the turbulence intensity is only controlled by the amplitude of shear flow and the bottom roughness, relying on the boundary condition. If we consider the situation in atmosphere, it could be much more complex. Indeed, the convection induced by the solar heating brings another source of turbulence, that may affect the velocity profile close to the surface as well as including the influence of sand and dust storms. Meanwhile, power law is used when surface softness or stability information is not available, even though, it is an empirical relation and without physical basis. It gives a simple
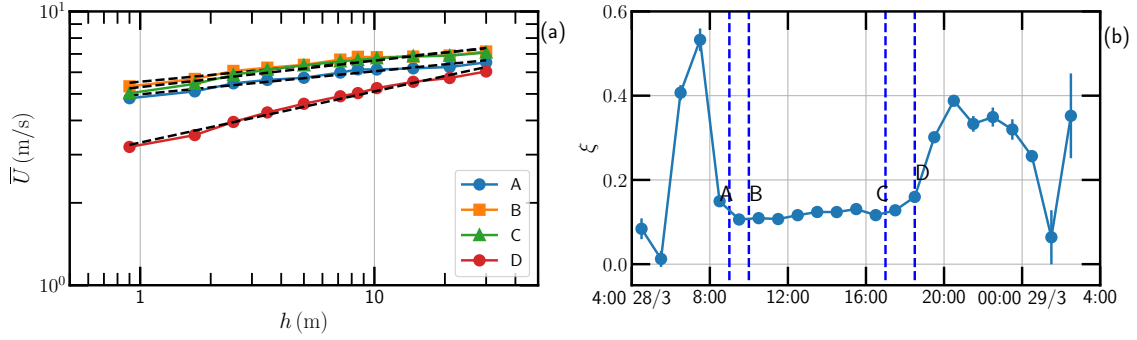
Figure 9. (a) Examination of the power-law relation, i.e., $\overline{U}(h) \propto h^\xi$, at four typical periods from A to D. The dashed line is a power-law fitting for reference. (b) Temporal evolution of the power-law scaling exponent ξ.

relationship between the wind speed at one height and those at another. Ten meter wind speed is used as the reference level, where the standard height prescribed by the WMO.

The power-law relation, i.e., $\overline{U}(h) \propto h^\xi$, has been proposed (Barenblatt, 1993; Zagarola et al., 1997; Chen and Liu, 2005). The scaling exponent ξ is expected to be constant for infinite Reynolds number (i.e., $Re = UL/\nu$ where U is the wind speed, L is the typical length scale, e.g., the height of the sensor location, and ν is the kinetic viscosity of air). It is interesting to note that the power-law relation is evident for the current dataset since the Reynolds number of the current data is up to $\mathcal{O}(10^7)$ (Fig. 9). It shows roughly a constant value $\xi = 0.12 \pm 0.01$ in the stabilizing stage, since the Reynolds number/wind speed in this period is nearly constant. Note that with such features, comparison of logarithmic wind profiles and power law wind profiles is possible.

6 Conclusions

The high frequency observatory data for studying the features of fluid and dust filed during sand and dust storms were presented. The complex physical process during the evolution of sand and dust storms is still unknown for the lack of massive atmospheric observation, especially for the high resolution and synchronous measurement near the surface. For a better understanding of the interplay between turbulent flows and non-turbulent motions during the SDS, the three-stage model was put forward to facilitate the easy understanding of the different fluid and dust features based on the mean velocity changes (also partially taking into consideration the wind direction, PM_{10} concentration, etc.). For the whole process during the SDS, gradually from ascending to stabilizing to descending effects in turbulent energy and structures was obtained through Fourier spectra, corresponding to the three-stage model. The features revealed in this work make us a deeper and wider understanding of the SDS fluid and dust field. It is anticipated that the data collected in this work will be of specific utility for the boundary layer community to build the model about sand and dust storm, but also more broadly for communities studying the exchange of dust and fluid field, and energy transfer for the particle laden two phase flow.

Code and data availability. The data set was uploaded to Zenodo with DOI 10.5281/zenodo.5034196 (Li et al., 2021a). The data sets are published under Creative Commons Attribution 4.0 International (CC BY 4.0) license. The Python scripts used in this study are available at https://github.com/lanlankai.

260   *Author contributions.* XJZ, GHW and XBL designed the experiment. XBL performed the field observations and data analyses as well as managed the manuscript, which was guided and edited by YXH, GHW and XJZ. All authors discussed the results and commented on the manuscript.

Competing interests. The authors declare that they have no conflict of interest.

Disclaimer. The data is provided as is with no warranties.

265   *Acknowledgements.* We thank Haihua Gu, Tianli Bo, Ao Mei, Guowen Han, Yirui Liang, Zhang Huan, Hongyou Liu, Haibo Yang, Haojie Huang and Xiaobin Zhang for providing useful assistance in the field observations. We acknowledge support from the National Natural Science Foundation of China (No. 92052202 and 11732010), and XBL is also supported by CSC scholarship (File No. 201706180037). YX is also partially supported by State Key Laboratory of Ocean Engineering (Shanghai Jiao Tong University) (Grant No. 1910). The data used in this study will be available in Zenodo data repository when it is accepted. Additional observation data may be requested from the 270   corresponding author.

References

Balakumar, B. and Adrian, R.: Large-and very-large-scale motions in channel and boundary-layer flows, Philos. T. R. Soc. A, 365, 665–681, https://doi.org/10.1098/rsta.2006.1940, 2007.

Banta, R. M., Pichugina, Y. L., and Brewer, W. A.: Turbulent velocity-variance profiles in the stable boundary layer generated by a nocturnal low-level jet, J. Atmos. Sci., 63, 2700–2719, https://doi.org/10.1175/jas3776.1, 2006.

Barenblatt, G. I.: Scaling laws for fully developed turbulent shear flows. Part 1. Basic hypotheses and analysis, J. Fluid Mech., 248, 513–520, https://doi.org/10.1017/S0022112093000874, 1993.

Bian, C., Liu, Z., Huang, Y., Zhao, L., and Jiang, W.: On Estimating Turbulent Reynolds Stress in Wavy Aquatic Environment, J. Geophys. Res. Oceans, 123, 3060–3071, https://doi.org/10.1002/2017JC013230, 2018.

Borbély-Kiss, I., Kiss, A., Koltay, E., Szabo, G., and Bozó, L.: Saharan dust episodes in Hungarian aerosol: elemental signatures and transport trajectories, J. Aerosol Sci., 35, 1205–1224, https://doi.org/10.1016/j.jaerosci.2004.05.001, 2004.

Chang, Y.-S., Arndt, R. L., and Carmichael, G. R.: Mineral base-cation deposition in Asia, Atmos. Environ., 30, 2417–2427, https://doi.org/10.1016/1352-2310(95)00196-4, 1996.

Chen, W. F. and Liu, E. M.: Handbook of structural engineering, CRC Press, 2nd edition edn., 2005.

Daubechies, I., Lu, J., and Wu, H.-T.: Synchrosqueezed wavelet transforms: an empirical mode decomposition-like tool, Appl. Comput. Harmon. Anal., 30, 243–261, https://doi.org/10.1016/j.acha.2010.08.002, 2011.

Davies, L. and Gather, U.: The identification of multiple outliers, J. Am. Stat. Assoc., 88, 782–792, https://doi.org/10.2307/2290763, 1993.

DeMott, P. J., Sassen, K., Poellot, M. R., Baumgardner, D., Rogers, D. C., Brooks, S. D., Prenni, A. J., and Kreidenweis, S. M.: African dust aerosols as atmospheric ice nuclei, Geophys. Res. Lett., 30, https://doi.org/10.1029/2003GL017410, 2003.

Flandrin, P.: Time-frequency/time-scale analysis, Academic Press, 1998.

Foken, T., Göockede, M., Mauder, M., Mahrt, L., Amiro, B., and Munger, W.: Post-field data quality control, in: Handbook of micrometeorology, pp. 181–208, Springer, 2004.

Frisch, U.: Turbulence: the legacy of AN Kolmogorov, Cambridge University Press, 1995.

Gao, Y., Arimoto, R., Duce, R., Zhang, X., Zhang, G., An, Z., Chen, L., Zhou, M., and Gu, D.: Temporal and spatial distributions of dust and its deposition to the China Sea, Tellus B: Chemical and Physical Meteorology, 49, 172–189, https://doi.org/10.3402/tellusb.v49i2.15960, 1997.

Gao, Y., Schmitt, F. G., Hu, J. Y., and Huang, Y. X.: Scaling Analysis of the China France Oceanography SATellite Along-Track Wind and Wave Data, J. Geophys. Res. Oceans, 126, e2020JC017 119, https://doi.org/10.1029/2020JC017119, 2021.

Goudie, A. S.: Dust storms: Recent developments, J. Environ. Manage., 90, 89–94, https://doi.org/10.1016/j.jenvman.2008.07.007, 2009.

Harrison, S. P., Kohfeld, K. E., Roelandt, C., and Claquin, T.: The role of dust in climate changes today, at the last glacial maximum and in the future, Earth Sci. Rev., 54, 43–80, https://doi.org/10.1016/s0012-8252(01)00041-1, 2001.

Hefflin, B. J., Jalaludin, B., McClure, E., Cobb, N., Johnson, C. A., Jecha, L., and Etzel, R. A.: Surveillance for dust storms and respiratory diseases in Washington State, 1991, Archives of Environmental Health: An International Journal, 49, 170–174, https://doi.org/10.1080/00039896.1994.9940378, 1994.

Holtslag, A.: Reference module in earth systems and environmental sciences: Encyclopedia of Atmospheric Series, Academic Press, second edition edn., 2015.

Huang, N. E., Shen, Z., Long, S. R., Wu, M. C., Shih, H. H., Zheng, Q., Yen, N.-C., Tung, C. C., and Liu, H. H.: The empirical mode decomposition and the Hilbert spectrum for nonlinear and non-stationary time series analysis, Proc. Rov. Soc. London A, 454, 903–995, https://doi.org/10.1098/rspa.1998.0193, 1998.

310 Huang, Y., Schmitt, F. G., Lu, Z., and Liu, Y.: An amplitude-frequency study of turbulent scaling intermittency using empirical mode decomposition and Hilbert spectral analysis, Europhys. Lett., 84, 40 010, https://doi.org/10.1209/0295-5075/84/40010, 2008.

Hutchins, N. and Marusic, I.: Evidence of very long meandering features in the logarithmic region of turbulent boundary layers, J. Fluid Mech., 579, 1–28, https://doi.org/10.1017/S0022112006003946, 2007.

Hutchins, N., Chauhan, K., Marusic, I., Monty, J., and Klewicki, J.: Towards reconciling the large-scale structure of turbulent boundary layers

315 in the atmosphere and laboratory, Boundary Layer Meteorol., 145, 273–306, https://doi.org/10.1007/s10546-012-9735-4, 2012.

Jickells, T., An, Z., Andersen, K. K., Baker, A., Bergametti, G., Brooks, N., Cao, J., Boyd, P., Duce, R., Hunter, K., et al.: Global iron connections between desert dust, ocean biogeochemistry, and climate, Science, 308, 67–71, https://doi.org/10.1126/science.1105959, 2005.

Kok, J. F., Parteli, E. J. R., Michaels, T. I., and Karam, D. B.: The physics of wind-blown sand and dust, Rep. Prog. Phys., 75, 106 901,

320 https://doi.org/10.1088/0034-4885/75/10/106901, 2012.

Kovasznay, L. S., Kibens, V., and Blackwelder, R. F.: Large-scale motion in the intermittent region of a turbulent boundary layer, J. Fluid Mech., 41, 283–325, https://doi.org/10.1017/S0022112070000629, 1970.

Lashermes, B., Jaffard, S., and Abry, P.: Wavelet leader based multifractal analysis, in: ICASSP 2005 Conference, Philadelphia, USA, https://doi.org/10.1109/ICASSP.2005.1415970, 2005.

325 Laurent, B., Marticorena, B., Bergametti, G., and Mei, F.: Modeling mineral dust emissions from Chinese and Mongolian deserts, Glob. Planet. Change, 52, 121–141, https://doi.org/10.1016/j.gloplacha.2006.02.012, 2006.

Leys, J. F., Heidenreich, S. K., Strong, C. L., McTainsh, G. H., and Quigley, S.: PM10 concentrations and mass transport during "Red Dawn"–Sydney 23 September 2009, Aeolian Res., 3, 327–342, https://doi.org/10.1016/j.aeolia.2011.06.003, 2011.

Li, X. and Bo, T.: An application of quadrant and octant analysis to the atmospheric surface layer, J. Wind Eng. Ind. Aerodyn., 189, 1–10,

330 https://doi.org/10.1016/j.jweia.2019.03.013, 2019a.

Li, X. and Bo, T.: Statistics and spectra of turbulence under different roughness in the near-neutral atmospheric surface layer, Earth Surf. Process. Landf., 44, 1460–1470, https://doi.org/10.1002/esp.4588, 2019b.

Li, X., Huang, Y., Wang, G., and Zheng, X.: High frequency observation during the sand and dust storms in the Qingtu Lake Observatory, https://doi.org/10.5281/zenodo.5034196, 2021a.

335 Li, X., Wang, G., and Zheng, X.: Study of coherent structures and heat flux transportation under different stratification stability conditions in the atmospheric surface layer, Phys. Fluids, 33, 065 113, https://doi.org/10.1063/5.0054205, 2021b.

Li, X., Wang, G., and Zheng, X.: Turbulent/Synoptic Separation and Coherent Structures in the Atmospheric Surface Layer for a Range of Surface Roughness, Boundary-Layer Meteorol, https://doi.org/10.1007/s10546-021-00643-z, 2021c.

Liu, H., Bo, T., and Liang, Y.: The variation of large-scale structure inclination angles in high Reynolds number atmospheric surface layers,

340 Phys. Fluids, 29, 035 104, https://doi.org/10.1063/1.4978803, 2017.

Liu, H., Wang, G., and Zheng, X.: Three-dimensional representation of large-scale structures based on observations in atmospheric surface layers, J. Geophys. Res. Atmos., 124, 10 753–10 771, https://doi.org/10.1029/2019JD030733, 2019.

Marusic, I., Mathis, R., and Hutchins, N.: Predictive model for wall-bounded turbulent flow, Science, 329, 193, https://doi.org/10.1126/science.1188765, 2010.

345   McCullough, M. and Kareem, A.: Testing stationarity with wavelet-based surrogates, J. Eng. Mech., 139, 200–209, https://doi.org/10.1061/(ASCE)EM.1943-7889.0000484, 2012.

McTainsh, G. and Pitblado, J.: Dust storms and related phenomena measured from meteorological records in Australia, Earth Surf. Process. Landf., 12, 415–424, https://doi.org/10.1002/esp.3290120407, 1987.

Monin, A. S.: The atmospheric boundary layer, Annu. Rev. Fluid Mech., 2, 225–250, https://doi.org/10.1146/annurev.fl.02.010170.001301,
350   1970.

Panofsky, H. A.: The atmospheric boundary layer below 150 meters, Annu. Rev. Fluid Mech., 6, 147–177, https://doi.org/10.1146/annurev.fl.06.010174.001051, 1974.

Shao, Y. and Dong, C.: A review on East Asian dust storm climate, modelling and monitoring, Global Planet. Change, 52, 1–22, https://doi.org/10.1016/j.gloplacha.2006.02.011, 2006.

355   Shi, Y., Shen, Y., Kang, E., Li, D., Ding, Y., Zhang, G., and Hu, R.: Recent and future climate change in northwest China, Clim. Change, 80, 379–393, https://doi.org/10.1007/s10584-006-9121-7, 2007.

Smits, A., McKeon, B., and Marusic, I.: High-Reynolds number wall turbulence, Annu. Rev. Fluid Mech., 43, 353–75, https://doi.org/10.1146/annurev-fluid-122109-160753, 2011.

Sokolik, I. N., Winker, D., Bergametti, G., Gillette, D., Carmichael, G., Kaufman, Y., Gomes, L., Schuetz, L., and Penner, J.: Introduction to
360   special section: Outstanding problems in quantifying the radiative impacts of mineral dust, J. Geophys. Res. Atmos., 106, 18 015–18 027, https://doi.org/10.1029/2000JD900498, 2001.

Stull, R. B.: An Introduction to Boundary Layer Meteorology, Kluwer Academic Publishers, 1997.

Sun, J., Mahrt, L., Nappo, C., and Lenschow, D. H.: Wind and temperature oscillations generated by wave–turbulence interactions in the stably stratified boundary layer, J. Atmos. Sci., 72, 1484–1503, https://doi.org/10.1175/jas-d-14-0129.1, 2015.

365   Terada, H., Ueda, H., and Wang, Z.: Trend of acid rain and neutralization by yellow sand in east Asia—a numerical study, Atmos. Environ., 36, 503–509, https://doi.org/10.1016/s1352-2310(01)00509-x, 2002.

Terradellas, E., Soler, M., Ferreres, E., and Bravo, M.: Analysis of oscillations in the stable atmospheric boundary layer using wavelet methods, Boundary Layer Meteorol., 114, 489–518, https://doi.org/10.1007/s10546-004-1293-y, 2005.

Uematsu, M., Duce, R. A., Prospero, J. M., Chen, L., Merrill, J. T., and McDonald, R. L.: Transport of mineral aerosol from Asia over the
370   North Pacific Ocean, J. Geophys. Res. Oceans, 88, 5343–5352, https://doi.org/10.1029/JC088iC09p05343, 1983.

UNESCAPReport: Sand and Dust Storms in Asia and the Pacific: Opportunities for Regional Cooperation and Action, Tech. rep., United Nations ESCAP, 2018.

Wang, G. and Zheng, X.: Very large scale motions in the atmospheric surface layer: a field investigation, J. Fluid Mech., 802, 464–489, https://doi.org/10.1017/jfm.2016.439, 2016.

375   Wang, G., Zheng, X., and Tao, J.: Very large scale motions and PM_{10} concentration in a high-Re boundary layer, Phys. Fluids, 29, 061 701, https://doi.org/10.1063/1.4990087, 2017.

Wang, G., Gu, H., and Zheng, X.: Large scale structures of turbulent flows in the atmospheric surface layer with and without sand, Phys. Fluids, 32, 106 604, https://doi.org/10.1063/5.0023126, 2020.

Wang, Q., Dong, X., Fu, J. S., Xu, J., Deng, C., Jiang, Y., Fu, Q., Lin, Y., Huang, K., and Zhuang, G.: Environmentally dependent dust
380   chemistry of a super Asian dust storm in March 2010: observation and simulation., Atmos. Chem. Phys., 18, https://doi.org/10.5194/acp-18-3505-2018, 2018.

Wu, Z., Huang, N. E., Long, S. R., and Peng, C.-K.: On the trend, detrending, and variability of nonlinear and nonstationary time series, Proc. Natl. Acad. Sci., 104, 14 889–14 894, https://doi.org/10.1073/pnas.0701020104, 2007.

Yin, S., Anpu, W., Shulan, Y., and Pingsheng, L.: Correlation of acid rain with the distributions of acid and alkaline elements in aerosols, Nucl. Instrum. Methods Phys. Res., Sect. B, 109, 551–554, https://doi.org/10.1016/0168-583X(95)00967-1, 1996.

Zagarola, M. V., Perry, A. E., and Smits, A. J.: Log laws or power laws: The scaling in the overlap region, Phys. Fluids, 9, 2094–2100, https://doi.org/10.1063/1.869328, 1997.

Zhang, H. and Zheng, X.: Quantifying the large-scale electrification equilibrium effects in dust storms using field observations at Qingtu Lake Observatory, Atmos. Chem. Phys., 18, 17 087–17 097, https://doi.org/10.5194/acp-18-17087-2018, 2018.

Zhang, H. and Zhou, Y.-H.: Effects of 3D electric field on saltation during dust storms: an observational and numerical study, Atmospheric Chem. Phys., 20, 14 801–14 820, https://doi.org/10.5194/acp-20-14801-2020, 2020a.

Zhang, H. and Zhou, Y.-H.: Reconstructing the electrical structure of dust storms from locally observed electric field data, Nat. Commun., 11, 1–12, https://doi.org/10.1038/s41467-020-18759-0, 2020b.

Zhou, C., Zhang, X., Zhang, J., and Zhang, X.: Representations of dynamics size distributions of mineral dust over East Asia by a regional sand and dust storm model, Atmos. Res., 250, 105 403, https://doi.org/10.1016/j.atmosres.2020.105403, 2021.

Zhuang, G., Yi, Z., Duce, R. A., and Brown, P. R.: Link between iron and sulphur cycles suggested by detection of Fe (n) in remote marine aerosols, Nature, 355, 537, https://doi.org/10.1038/355537a0, 1992.

Zoljoodi, M., Didevarasl, A., and Saadatabadi, A. R.: Dust events in the western parts of Iran and the relationship with drought expansion over the dust-source areas in Iraq and Syria, Clim. Atmos. Sci., 3, 321, https://doi.org/10.4236/acs.2013.33034, 2013.